Available online at www.sciencedirect.com
ScienceDirect
Trans. Nonferrous Met. Soc. China 32(2022) 472−482
Transactions of Nonferrous Metals Society of China
www.tnmsc.cn

Enhanced Mg/graphene interface adhesion using intermediate MgO layers: First-principles prediction and analysis

Wei-cheng WANG[1*], Jin-long LIU[1*], Han-han ZHAO[1], Qiu-hong YUAN[2], Lan LUO[1,3], Yong JIANG[4], Yong LIU[1]

1. Key Laboratory of Lightweight and High Strength Structural Materials of Jiangxi Province, Nanchang University, Nanchang 330031, China;
2. Physical Science and Technology College, Yichun University, Yichun 336000, China;
3. School of Materials Science and Engineering, Nanchang University, Nanchang 330031, China;
4. School of Materials Science and Engineering, Central South University, Changsha 410083, China

Received 14 January 2021; accepted 29 June 2021

Abstract: Graphene-reinforced Mg matrix composites suffer seriously from the weak Mg/graphene interfacial bonding. In this study, a first-principles study was performed to evaluate the feasibility of improving the Mg/graphene bonding using an in-situ formed intermediate MgO layer. The calculated interface adhesion strengths suggested a relative ordering (from high to low) of Mg(0001)/MgO($1\bar{1}1$) > MgO($1\bar{1}1$)/graphene > Mg(0001)/graphene. The enhanced Mg/MgO/graphene interface bonding can be attributed to the newly formed strong ionic and covalent interactions at the Mg/MgO and the MgO/graphene interfaces, respectively, which replace the otherwise very weak van der Waals bonding between Mg and graphene.

Key words: magnesium matrix composite; graphene; MgO; interface; first-principles

1 Introduction

Magnesium (Mg) alloys are known for their excellent combination of light mass, high specific strength and stiffness [1−3]. However, massive engineering applications of magnesium alloys still suffer seriously from their relative low strength and poor ductility [4−7]. Magnesium matrix composites (MMCs) dispersed with discontinuous reinforcements (short fibers, whiskers or particles) exhibit great promises for their remarkably improved strength [8,9]. Nano-carbons, such as carbon nano-tubes (CNTs) and graphene nano-sheets (GNSs), have been considered as reinforcements during decades, due to their exceptional mechanical properties and thermal conductivities [10]. Numerous experimental evidences verified that CNT and GNS reinforcements can significantly improve the elastic modulus, yield strength, and ultimate tensile strength, but often with the sacrifice of elongation and ductility [11−14]. The proper balance between high strength and good ductility of these MMCs faces the challenges from the intrinsically very weak Van Der Waals bonding between nano-carbons and Mg [15,16].

The interfacial bonding that governs the structural and chemical stabilities of nano-carbons in Mg must be greatly improved for developing high-performance MMCs [10]. Various interface modification methods have been proposed in hopes to improve the adhesion of nano-carbons in Mg and hence the overall mechanical performance of the

Corresponding author: Yong LIU, E-mail: liuyong@ncu.edu.cn; Yong JIANG, E-mail: yjiang@csu.edu.cn
*Wei-cheng WANG and Jin-long LIU contributed equally to this work
DOI: 10.1016/S1003-6326(22)65808-4

MMCs [17−22]. For instance, coating CNTs with Si or Ni increased both the strength and plasticity for a CNT-reinforced Mg matrix composite [17−19]. Coating GNSs with Ni also led to higher wear resistance and fracture toughness for a GNS-reinforced Mg alloy (AZ31) [21]. Nevertheless, benefits resulted from such element decoration techniques are found to be very limited. Recalling that both nano-carbons and Mg are prone to oxidation, it is thus strongly suggested that the native oxide of Mg (i.e. MgO) could act as an intermediate adhesive layer, to efficiently bind with both nano-carbons and the Mg matrix through its unsaturated surface oxygen atoms. In one of our early studies, we have testified MgO as the intermediate layer for this purpose [23]. CNTs were chemically deposited with a layer of MgO and then mixed with Mg, which can dramatically improve the yield strength and elongation by 69% and 23%, respectively, as compared to the AZ91 alloy matrix [24]. Later on, we improved such technique by forming in-situ MgO nano-particles at GNS/Mg interfaces through local thermal reduction of oxidized GNSs inside the AZ91 alloy [8,25]. The in-situ modified GNSs showed a more uniformly distribution in Mg, and the yield strength and elongation were increased to a high record, by up to 85.7% and 61.4%, respectively [8].

All these studies strongly suggested that the bonding of Mg/MgO and MgO/GNS can be both intrinsically superior to that of the Mg/GNS interfaces, but the fundamental mechanisms have never been clarified. First-principles interface calculation is an indispensable tool for exploring such fundamental aspects at the electronic and atomic levels. The chemical interaction and valence charge transfer between graphene and a series of pure metal matrices have been thoroughly studied from the first-principles [26]. It was also predicted by first-principles calculation that doping with certain transition metals (Cr and Ti) could enhance the Cu/graphene interface adhesion [27]. There also existed a first-principles calculation on the adhesion of MgO single-crystals in molten Mg [28] which employed an arbitrary Mg/MgO orientation relation (OR) of $(0001)[10\bar{1}0]_{Mg} // (111)[1\bar{1}0]_{MgO}$. This OR, however, could deviate significantly from the Mg/MgO OR in solid state MMCs.

In this work, based on the experimentally observed OR, first-principles calculation was performed to explore the intrinsic bonding natures of the Mg/MgO and MgO/graphene interfaces. The results were then compared with the clean Mg/graphene interface, to elucidate the critical roles of MgO intermediate layers in enhancing the Mg/graphene interface adhesion. Such interface modification strategy can be extended to improve many other heterogeneous interface systems that suffer from their intrinsically-weak interfacial bonding.

2 Methodology

2.1 Experimental methods

The commercial available AZ91 alloy powders which have an average particle size of about 70 mm and 99.9% in purity were used. The natural graphite powders (99.99%) and the analytical reagents were used to prepare GNS. Graphene oxide (GO) prepared by a modified Hummers method [29] was used to synthesize the GNS. The GO powders mounted on a crucible were introduced into a tube furnace and thermally treated at 873 K for 20 min under a flow of laminar Ar (99.99%). The Ar flow rate and heating rate were 303 K/min and 30 mL/min, respectively [25].

To effectively disperse GNS in the alloy matrix, the ultrasonic processing was conducted with a vibration frequency of 100 kHz. The GNSs were dispersed into ethanol by ultrasonication for 2 h. AZ91 powders were added in ethanol under the argon atmosphere with the following ultra-sonicating for 30 min to obtain a suspension of AZ91 powders. The mixed suspension was then simultaneously mechanical-stirred and ultra-sonicated for 1 h, and then filtered and dried under vacuum to obtain the AZ91−GNS mixtures. After that, the mixtures were pressed, sintered and hot-extruded with the following T4 treatment. Detailed information may be found in Ref. [24]. A AZ91−GNS composites have been successfully fabricated, and the interface structures relevant to in-situ formed intermediate MgO layers have been characterized for an AZ91 alloy reinforced by oxidized GNSs using HRTEM [25].

2.2 Computational methods

All first-principles density functional theory (DFT) calculations were performed using the semi-commercial code, i.e. Vienna Ab-initio

Simulation Package (VASP), with the plane-wave basis sets and periodic boundary conditions [30,31]. The Blöchl projector augmented wave method (PAW) within the frozen-core approximation [32] was used to describe the ion−electron interactions. The exchange-correlation functions were treated using generalized gradient approximation (GGA) of Perdew−Burke−Ernzerhof (PBE) [33]. The electronic structures of Mg, O, and C are $2s^2 2p^6 3s^2$, $1s^2 2s^2 2p^4$, and $1s^2 2s^2 2p^2$, respectively. For the structural relaxation calculations, the self-consistence convergence criterion for electron iterations was set to be 10^{-5} eV, and the ground-state atomic geometries were optimized by minimizing the Hellman−Feymman force on each ion to less than 0.02 eV/Å. For the conventional cells of Mg, MgO, and graphene, a high energy cutoff of 480 eV and a Monkhorst-Pack *k*-mesh of 5 × 5 × 4, 5 × 5 × 5, and 5 × 5 × 2 were found to be sufficient, respectively, for achieving the total energy convergence of the system within 1 meV/atom. The optimized lattice parameters of Mg, MgO, and graphene after relaxation are listed in Table 1. For the interface supercell of Mg(0001)/ MgO(1 $\bar{1}$1), MgO(1 $\bar{1}$1) /graphene, and Mg(0001)/graphene, a high energy cutoff of 480 eV and a Monkhorst-Pack *k*-mesh of 15 × 15 × 1, 5 × 9 × 1, and 3 × 3 × 1 were found to be sufficient, respectively. Moreover, long-range dispersion interaction associated with graphene multilayers was considered using the semi- empirical van der Waals energy correction within the DFT-D2 scheme [34].

Table 1 Optimized lattice parameters of Mg, MgO, and graphene and their space groups

Phase	*a*/Å	*c*/Å	Space group
Mg	3.181	5.218	$p6_3/mmc$ (No.194)
MgO	4.241	−	$fm\bar{3}m$ (No.225)
Graphene	2.469	6.837	$p6_3/mmc$ (No.194)

3 Results and discussion

3.1 Interface modeling

Figure 1(a) shows the HRTEM image of the resulting *α*-Mg/MgO/GNS interfaces. The GNSs remain undestroyed during fabrication. The interlayer spacing of graphene sheets is measured to be 0.334 nm, which is very close to that of initial GNSs [35]. Figure 1(b) shows the inverse Fourier-filtered image of *α*-Mg/MgO interface with the inverse Fast-Fourier-Transform (FFT) patterns of *α*-Mg (top) and MgO (bottom). This interface exhibits good coherency. The most densely-packed planes of $(0002)_{\alpha\text{-Mg}}$ and $(1\,\bar{1}\,1)_{\text{MgO}}$ are essentially parallel, with a small tilt angle of ~6°. The most densely-packed directions of $[01\,\bar{1}0]_{\alpha\text{-Mg}}$ and $[0\,\bar{1}\,1]_{\text{MgO}}$ also align to each other. The OR between *α*-Mg and MgO can be thus determined as $(0002)[01\,\bar{1}0]_{\alpha\text{-Mg}} // (1\,\bar{1}\,1)[0\,\bar{1}\,1]_{\text{MgO}}$. Figure 1(c) shows the inverse Fourier-filtered image of the MgO/GNS interface. Lattice distortion is evidently seen in the

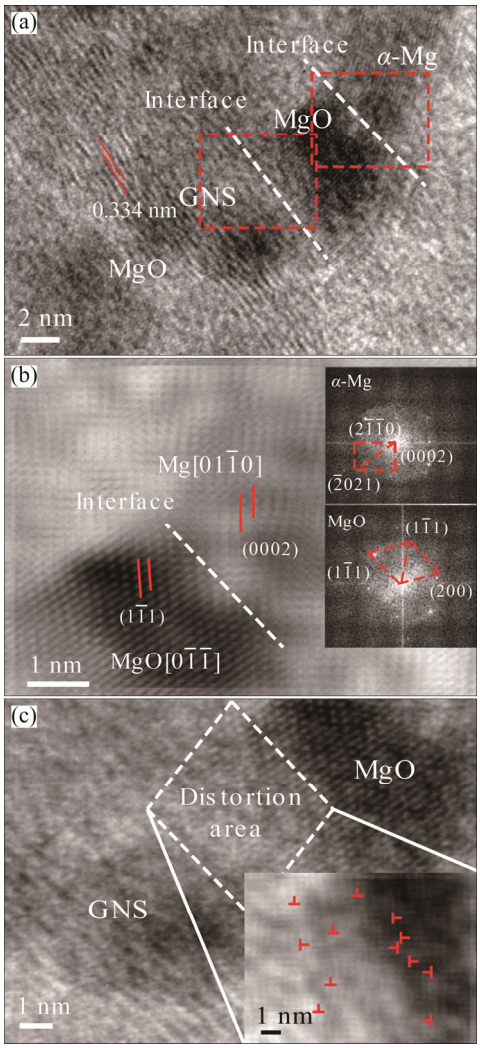

Fig. 1 HRTEM image of *α*-Mg/MgO/GNS interfaces (a), inverse Fourier-filtered images of *α*-Mg/MgO (b) and MgO/GNS (c) interfaces in (a) (The insets in (b) are the FFT patterns of *α*-Mg (top) and MgO (bottom), and the inset in (c) shows a high magnification image of the distortion region between MgO and GNS nanoparticles) (Reprinted with permission from Ref. [25])

interfacial region between GNSs and MgO nanoparticles. The distortion regions are featured with a high density of dislocations. For that the MgO nanoparticles are directly resulted from the local in-situ thermal reduction of oxidized GNSs by Mg, an atomic-resolution structure of this interface can be hardly obtained, but, still very clearly, MgO interfaces with graphene through its $(1\bar{1}1)$ facets.

Based on the experimental OR of $(0002)[01\bar{1}0]_{\alpha\text{-Mg}} // (1\bar{1}1)[0\bar{1}1]_{MgO}$, the atomic structures of the Mg(0001)/MgO($1\bar{1}1$) interface were constructed in Fig. 2. Using surface energy convergence tests, seven layers of Mg(0001) (1×1) and thirteen layers of MgO($1\bar{1}1$) (1×1) were found to be sufficient for constructing the Mg/MgO interface supercell models. To accommodate the lattice mismatch at the interface, the Mg(0001) slab was compressed and the MgO($1\bar{1}1$) slab was stretched by about the same amount, ~3.0%. The MgO($1\bar{1}1$) surface may have two different surface terminations, i.e. the O-terminated and the Mg-terminated. Depending on how to place the surface Mg atoms of the Mg(0001) relative to the MgO($1\bar{1}1$), each termination can further correspond to three different coordination types, i.e. the on-top, the hcp-hollow, and the fcc-hollow. Therefore, a total of six possible atomic structures can be resulted for modelling the Mg(0001)/MgO($1\bar{1}1$) interface in Fig. 2. In order to show the coordination relationship of atoms at the interface, the top views of these interface models are also provided at the bottom.

Similarly, seven layers of MgO($1\bar{1}1$) $(3\times\sqrt{3})$ and three layers of graphene $(2\sqrt{3}\times2)$ were adopted to construct the MgO($1\bar{1}1$)/graphene interface supercell models. Again, to accommodate the lattice mismatch at the interface, the MgO($1\bar{1}1$) slab was stretched the same as that

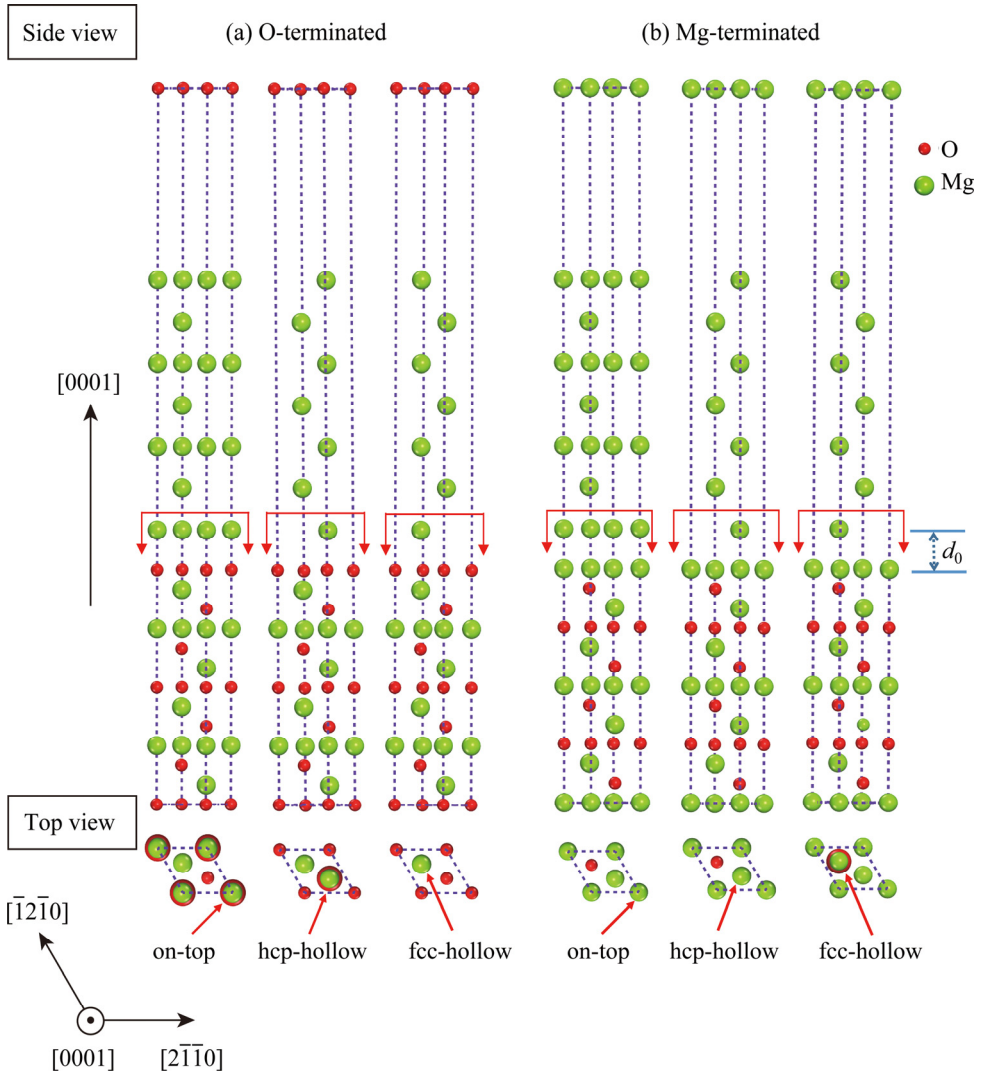

Fig. 2 Atomic structures of Mg(0001)/MgO($1\bar{1}1$) interfaces with different terminations and coordination types

at the Mg(0001)/MgO(1$\bar{1}$1) interface and the graphene slab was compressed accordingly by ~6.47%. For the O-terminated MgO(1$\bar{1}$1)/graphene interface, we considered two coordination types, i.e. the bridge (OB) or the top and hollow (OTH), by aligning the outmost O atoms of the MgO(1$\bar{1}$1) to the bridge sites or the top and hollow sites of the top graphene sheet, respectively. Other two coordination types, i.e. the bridge (MB) and top and hollow (MTH), were also constructed in the similar manner for modelling the Mg-terminated interface counterpart. Therefore, a total of four possible atomic structures can be resulted for modelling the MgO(1$\bar{1}$1)/graphene interface in Fig. 3.

Figure 4 shows the atomic structure of the clean Mg(0001)/graphene interface without the impact of the intermediate MgO(1$\bar{1}$1) layers. The supercell contains six layers of Mg(0001) (3 × 3) and three layers of graphene (4 × 4). Each Mg or graphene layer consists of 9 Mg atoms or 32 C atoms, respectively. Again, to accommodate the lattice mismatch at the interface, the Mg(0001) slab was stretched and the graphene slab was compressed by about the same amount, ~1.09%. The resulting coordination can be clearly seen in the top view in Fig. 4. Among the 9 Mg atoms of the top Mg(0001) layer, two are positioned at the top sites, one at a hollow site, and the rest at the bridge sites of graphene. For all the above supercells, a vacuum thickness of at least 12 Å was imposed to avoid any possible interactions across the vacuum.

3.2 Interface adhesion strength

The first-principles adhesion strength of an interface can be evaluated by the work of separation (W_{sep}). W_{sep} measures the energy input to rigidly break the interface into two halves with an infinite separation. Two approaches for W_{sep} exist. First, the work of separation can be calculated using the UBER (universal binding energy relation) method [36] through Eq. (1):

$$E(d)=-E_0(1+\frac{d-d_0}{l})\exp(\frac{d_0-d}{l}) \quad (1)$$

where $E(d)$ is the calculated total energy of the interface per unit interface area at a given interface separation d; E_0 is the equilibrium adhesion energy, i.e. the ideal work of separation W_{sep}^0, of the interface; d_0 is the equilibrium interface separation; l is the scaling length.

For each interface structure in Figs. 2−4, a series of $E(d)$ data were obtained by DFT calculations without relaxation. By fitting the $E(d)$ data into the UBER equation in Fig. 5, one can solve out the equilibrium interface separation d_0 and the ideal work of separation W_{sep}^0 of the Mg(0001)/MgO(1$\bar{1}$1), the MgO(1$\bar{1}$1)/graphene and the Mg(0001)/graphene interfaces, respectively. The corresponding results are summarized in Table 2.

Alternatively, the work of separation of an interface can be directly calculated as

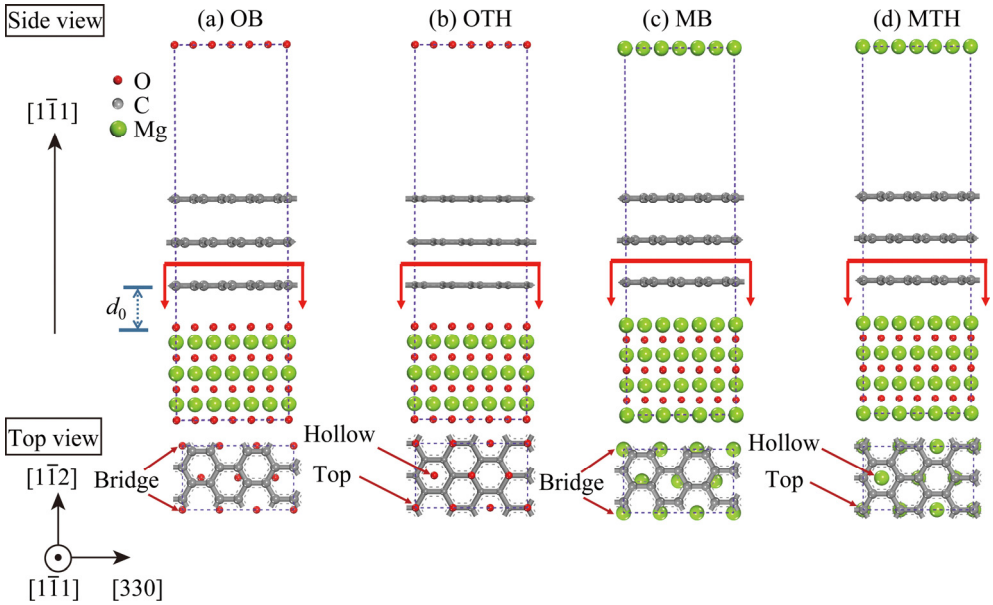

Fig. 3 Atomic structures of MgO(1$\bar{1}$1)/graphene interfaces with different terminations and coordination types

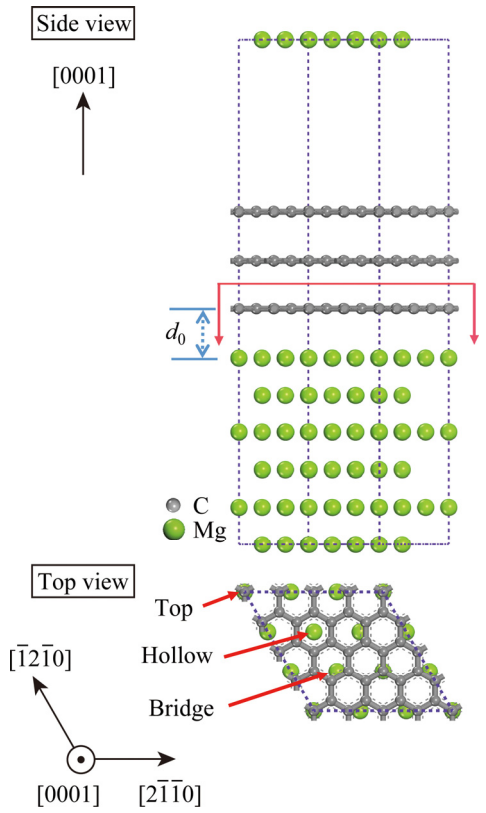

Fig. 4 Atomic structure of Mg(0001)/graphene interface

$$W_{\text{sep}}(A/B)=\frac{E_A^{\text{slab}}+E_B^{\text{slab}}-E_{\text{tot}}^{\text{intf}}}{A} \quad (2)$$

where $E_{\text{tot}}^{\text{intf}}$ is the total energy of the fully relaxed interface supercell at its equilibrium state. E_A^{slab} and E_B^{slab} are the total energies of the two halves individually evaluated in the same size supercell, respectively. A is the cross-section area of the interface. Positive W_{sep} indicates an energy-favored interface structure and the value of W_{sep} measures the adhesion strength. The corresponding results are also compared in Table 2.

The following findings can be suggested by Table 2. Firstly, the two approaches always predict similar results for both W_{sep} and d_0, no matter the interface structure type. Secondly, all W_{sep} values are predicted as positive, indicating that all these interface structures could be favored in energy. Among which, the O-terminated Mg(0001)/MgO(1 $\bar{1}$ 1) interfaces have extremely strong adhesion strength (W_{sep}=7−11 J/m^2), depending on the specific coordination type. The strongest interfacial bonding is found for the fcc-hollow coordinated, O-terminated interface (i.e. the O-fcc) of Mg(0001)/MgO(1 $\bar{1}$ 1). In contrast, O-terminated

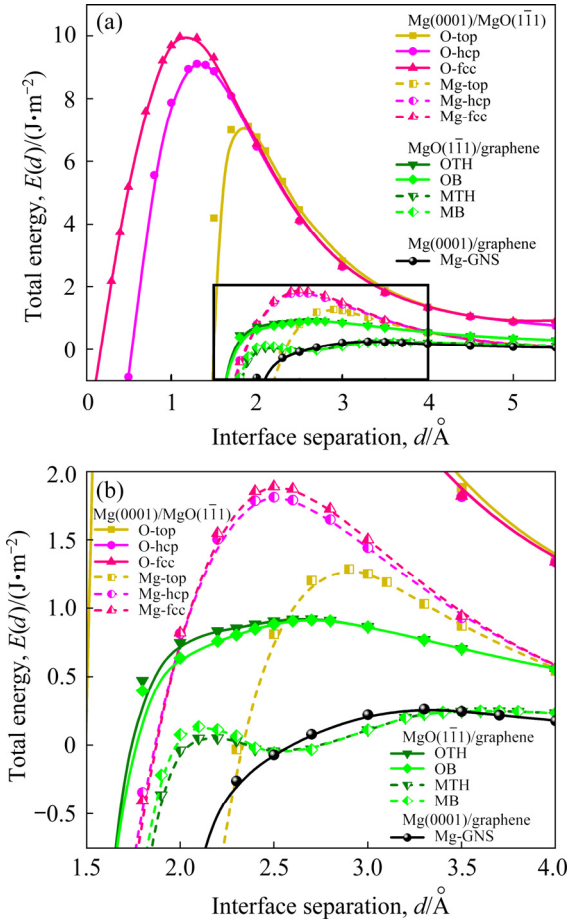

Fig. 5 UBER fitting of $E(d)$ data for Mg(0001)/MgO(1 $\bar{1}$ 1), MgO(1 $\bar{1}$ 1)/graphene and Mg(0001)/graphene interfaces (a), and magnified view (b) of frame region in (a)

MgO(1 $\bar{1}$ 1)/graphene interfaces are much weak, only W_{sep}≈1 J/m^2, but nevertheless, are much stronger than the Mg(0001)/graphene interface (W_{sep}≈0.25 J/m^2). Thirdly, compared to interfacial coordination, interfacial termination has a decisive impact on adhesion strength of the interface. W_{sep} can vary by four to ten folds among different termination types but by no more than 50% among different coordination types.

The most striking finding in Table 2 is that the intrinsically very weak bonding of the Mg/graphene interface (W_{sep}≈0.25 J/m^2) could be greatly enhanced up to four folds by introducing an intermediate MgO layer. The adhesion strength of the resulting Mg/MgO/graphene interfaces is thus essentially restricted to that of the MgO(1 $\bar{1}$ 1)/graphene interface, with W_{sep}≈1 J/m^2. This is likely the case that we achieved via local thermal reduction of oxidized GNSs in the GNS-reinforced AZ91 alloy [8,25]. The interface strengthening that

stems from the in-situ formed intermediate MgO layers not only achieved a more uniform distribution of GNSs in the Mg matrix (due to the much better wettability of MgO in Mg), but also improved the yield strength and elongation to a high record, by up to 85.7% and 61.4%, respectively, as compared to the AZ91 alloy [8].

3.3 Interfacial bonding natures

To clarify the bonding nature and the mechanisms responsible for adhesion performance of the investigated interfaces, we further performed electronic charge density, differential charge density, and density of states (DOS) analyses on these interfaces.

Enlightened by the calculation in Table 2, we selected the most energy-favored structures of the Mg(0001)/MgO(1$\bar{1}$1), the MgO(1$\bar{1}$1)/graphene and the Mg(0001)/graphene interfaces for charge density analyses firstly. Figure 6 compares the calculated total charge density contours of the near-interface areas, where the red and blue regions represent high and low charge density areas, respectively. Recalling that the charge densities within ionic cores are physically meaningless due to the use of pseudo-potentials in our DFT calculations, we thus need focus on the interstitial regions only.

Very clearly in Fig. 6(a), the charge density distribution in the α-Mg half shows a delocalized metallic bonding nature. When the interface is formed, the surface Mg atoms are strongly attracted

Table 2 Work of separation (W_{sep}) and equilibrium interface spacing (d_0) predicted by UBER method and full relaxation calculations

Interface structure	Termination and coordination type	UBER method		Full relaxation calculation	
		d_0/Å	W_{sep}/(J·m^{-2})	d_0/Å	W_{sep}/(J·m^{-2})
MgO(1$\bar{1}$1)/Mg(0001)	O-top	1.84	7.17	1.82	7.02
	O-hcp	1.28	9.12	1.21	10.18
	O-fcc	1.08	9.63	1.13	10.74
	Mg-top	2.88	1.27	2.86	1.3
	Mg-hcp	2.5	1.8	2.51	1.79
	Mg-fcc	2.5	1.88	2.51	1.88
MgO(1$\bar{1}$1)/graphene	OTH	2.48	0.94	1.98	1.23
	OB	2.57	0.98	2.36	1.1
	MTH	3.63	0.24	3.54	0.24
	MB	3.66	0.25	3.55	0.26
Mg(0001)/graphene		3.32	0.25	3.22	0.26

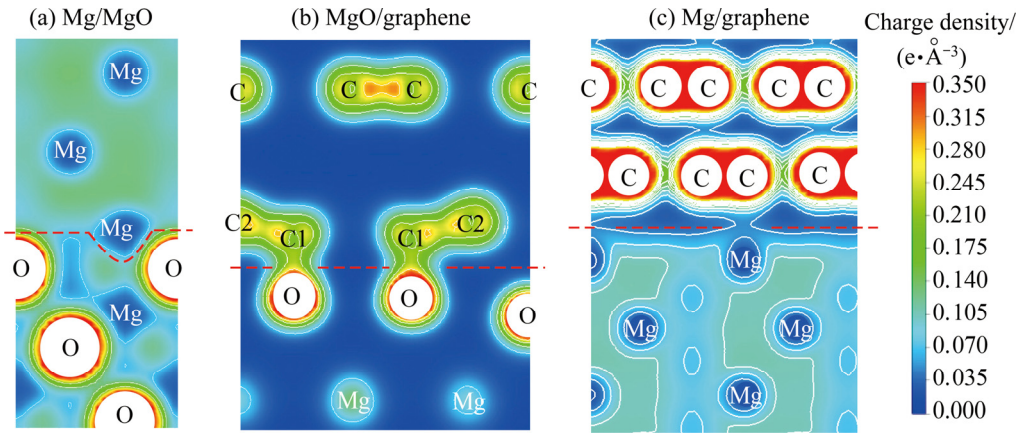

Fig. 6 Total charge density contours of Mg(0001)/MgO(1$\bar{1}$1) (O-fcc) (a), MgO(1$\bar{1}$1)/graphene (OTH) (b), and Mg(0001)/graphene (c) interfaces (The dashed lines denote the locations of the interfaces)

to the fcc-hollow-sites of the O-terminated MgO(1$\bar{1}$1) surface until reaching the reasonable ionic interaction distance with the top-most O atoms with the highest W_{sep} of ~10 J/m^2.

For the MgO(1$\bar{1}$1)/graphene interface shown in Fig. 6(b), the top-most O atoms of the MgO are strongly attracted to the graphene layers, making the corresponding C1 atoms move downward. Consequently, some amounts of charges are built up between the interfacial O and C1 atoms, indicating the formation of C1—O covalent bonds across the interface. Meantime, the essentially zero charge density is also evident in the interface interstitial regions. The moderate adhesion strength is thus obtained, with W_{sep}≈1 J/m^2.

For the Mg(0001)/graphene interface, the charge density contour in Fig. 6(c) shows only minor charge accumulation between the Mg atoms and the corresponding C atoms, as a sign of very weak covalent Mg—C interaction. The charge density in other interfacial regions is equal to nearly zero. Very clearly, the interfacial charge density between Mg and graphene is comparable to that in the graphene interlayers, suggesting that the Mg/graphene bonding is at nearly the same level of the interlayer van der Waals forces in GNSs. Similar finding has been predicted for the interaction between graphene and many other metals [37]. As a result, the graphene layers are nearly untouched when forming the interface, yielding the weakest interface adhesion with W_{sep}≈0.25 J/m^2 only.

Based on the calculated charge densities and W_{sep} values, the benefits of intermediate MgO layers on enhancing the intrinsically weak Mg/graphene interface have been strongly manifested. To further elucidate the chemical bonding of the Mg(0001)/MgO(1$\bar{1}$1) and MgO(1$\bar{1}$1)/graphene interfaces, we calculated the corresponding differential charge densities and *l*-projected partial density of states shown in Figs. 7 and 8, respectively.

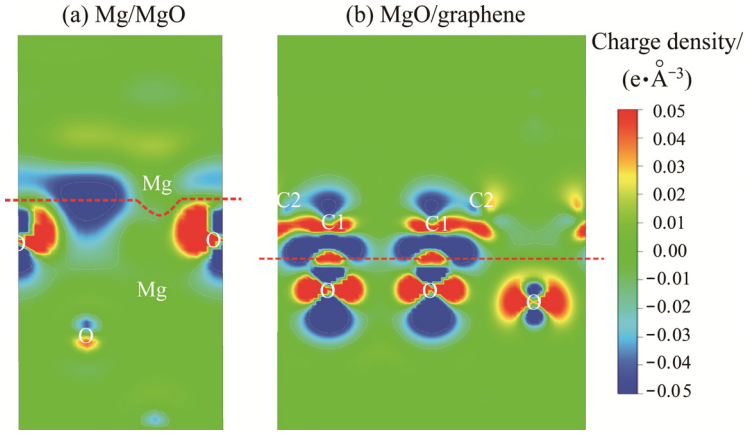

Fig. 7 Differential charge density distributions of Mg(0001)/MgO(1$\bar{1}$1) (O-fcc) (a) and MgO(1$\bar{1}$1)/graphene (OTH) (b) interfaces

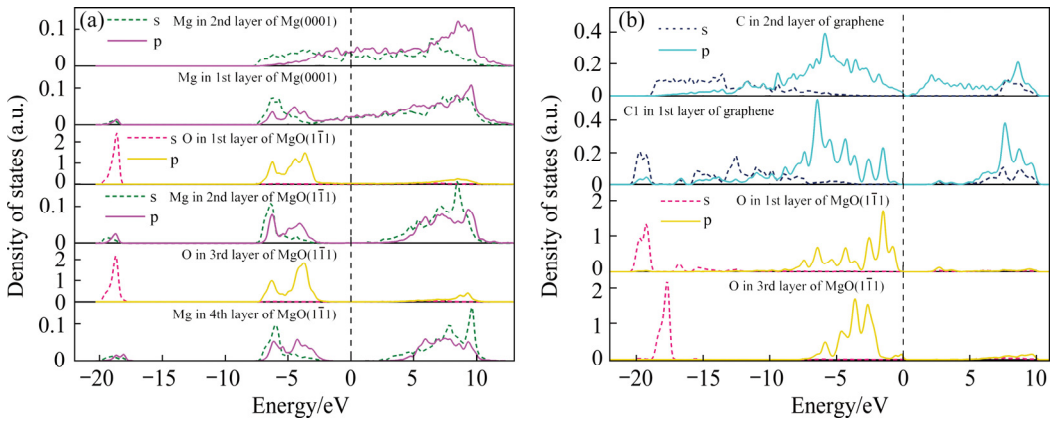

Fig. 8 *l*-projected partial density of states of Mg(0001)/MgO(1$\bar{1}$1) (O-fcc) (a) and MgO(1$\bar{1}$1)/graphene (OTH) (b) interfaces

For the Mg(0001)/MgO($1\bar{1}1$) interface in Figs. 7(a) and 8(a), the s-state hybridization between the outmost Mg(0001) atoms and the outmost O atoms of MgO($1\bar{1}1$) occurs mainly from −20 to −18.5 eV and from −7.5 to −5 eV, and p-state hybridization occurs mainly from −7.5 to −2.5 eV. The strong interaction with the outmost Mg atoms can even induce the p-orbital splitting of the outmost O atoms of MgO($1\bar{1}1$). As a result, the behaviors of the p_z-like orbital can be distinctively different from other p orbitals. This can be clearly seen in Fig. 7(a) that the O p_z-like orbitals gain electrons from the Mg side while some lose electrons. The net effect brings about strong ionic bonding characteristics to the interface. As a result, the DOS spectrum of the outmost Mg atoms differs obviously from that of the inner Mg atoms, and instead, becomes closer to the inner Mg atoms in MgO.

As for the MgO($1\bar{1}1$)/graphene interface in Figs. 7(b) and 8(b), the top-most O interacts strongly with the nearest neighboring C1 through their sp-orbitals. The DOS spectrum of the C1 atom differs significantly from the inner C atoms. The charge accumulation occurs in the intermediate region between the two atoms, reflecting the covalent bonding nature of C1—O. The s-state hybridization occurs mainly from −21 to −18.5 eV, and the p-state hybridization occurs mainly from −8 to 0 eV. The sp hybridization of C1 is also affected largely by the interaction with the O s-states. Compared to the inner O atoms, the s-states of the outmost O of MgO($1\bar{1}1$) shift significantly to lower energies, and the p-orbital splitting and band widening are also evident for the outmost O as seen in Figs. 7(b) and 8(b). In other interfacial region, the charge distribution remains unaffected.

4 Conclusions

(1) The work of separation (W_{sep}) values predicted by UBER fitting and full relaxation calculations are favorably comparable. The interface adhesion strength follows the relative ordering (from high to low) of Mg(0001)/MgO($1\bar{1}1$) > MgO($1\bar{1}1$)/graphene > Mg(0001)/graphene, with W_{sep} values of ~10, ~1, and ~0.25 J/m^2, respectively.

(2) The strong interface adhesion of the Mg(0001)/MgO($1\bar{1}1$) is majorly contributed by the strong ionic interaction between the outmost Mg(0001) atoms and the outmost O atoms of MgO($1\bar{1}1$). The modest adhesion strength of MgO($1\bar{1}1$)/graphene interface can be largely attributed to the covalent bonding between C and the topmost O atoms of MgO($1\bar{1}1$). The Mg/graphene interface is very weak due to the weak interaction between Mg and C, and the adhesion strength is comparable to the interlayer Van der Waals forces in GNSs.

(3) By replacing the weak Mg—C interaction with stronger C—O covalent bonding, the in-situ formed intermediate MgO layers can increase the interface adhesion by up to four folds.

Acknowledgments

The authors are grateful for the financial supports from the National Natural Science Foundation of China (Nos. 52061028, 52061039, 51971249, 51761037), the Natural Science Foundation of Jiangxi Province, China (No. 2020BABL204002), the Interdisciplinary Innovation Fund of Nanchang University (IIFNCU), China (No. 9166-27060003-ZD05), and the Innovative Funding for Graduate Students in Nanchang University, China (No. CX2019068).

References

[1] WANG X J, XU D K, WU R Z, CHEN X B, PENG Q M, JIN L, XIN Y C, ZHANG Z Q, LIU Y, CHEN X H, CHEN G, DENG K K, WANG H Y. What is going on in magnesium alloys? [J]. Journal of Materials Science & Technology, 2018, 34: 245−247.

[2] ZHANG Jing-huai, LIU Shu-juan, WU Rui-zhi, HOU Le-gan, ZHANG Mi-lin. Recent developments in high-strength Mg−RE-based alloys: Focusing on Mg−Gd and Mg−Y systems [J]. Journal of Magnesium and Alloys, 2018, 6: 277−291.

[3] TAYLOR S, WEST G D, MOGIRE E, TANG F, KOTADIA H R. Superplastic forming characteristics of AZ41 magnesium alloy [J]. Transactions of Nonferrous Metals Society of China, 2021, 31: 648−654.

[4] WANG Nai-guang, WANG Ri-chu, PENG Chao-qun, HU Cheng-wang, FENG Yan, PENG Bing. Research progress of magnesium anodes and their applications in chemical power sources [J]. Transactions of Nonferrous Metals Society of China, 2014, 24: 2427−2439.

[5] DUAN Meng, LUO Lan, LIU Yong. Microstructural evolution of AZ31 Mg alloy with surface mechanical attrition treatment: Grain and texture gradient [J]. Journal of Alloys and Compounds, 2020, 823: 153691.

[6] ZHONG Feng, WU Hua-jie, JIAO Yun-lei, WU Rui-zhi, HOU Le-gan, ZHANG Mi-lin. Effect of Y and Ce on the microstructure, mechanical properties and anisotropy of as-rolled Mg−8Li−1Al alloy [J]. Journal of Materials Science & Technology, 2020, 39: 124−134.

[7] AHMADI S, ALIMIRZALOO V, FARAJI G, DONIAVI A. Properties inhomogeneity of AM60 magnesium alloy processed by cyclic extrusion compression angular pressing followed by extrusion [J]. Transactions of Nonferrous Metals Society of China, 2021, 31: 655−665.

[8] YUAN Qiu-hong, QIU Zhi-qiang, ZHOU Guo-hua, ZENG Xiao-shu, LUO Lan, RAO Xi-xin, DING Yan, LIU Yong. Interfacial design and strengthening mechanisms of AZ91 alloy reinforced with in-situ reduced graphene oxide [J]. Materials Characterization, 2018, 138: 215−228.

[9] LI Qian-qian, ROTTMAIR C A, SINGER R F. CNT reinforced light metal composites produced by melt stirring and by high pressure die casting [J]. Composites Science and Technology, 2010, 70: 2242−2247.

[10] BAKSHI S R, LAHIR D, AGARWAL A. Carbon nanotube reinforced metal matrix composites — A review [J]. International Materials Reviews, 2010, 55: 41−64.

[11] SHIMIZU Y, MIKI S, SOGA T, ITOH I, TODOROKI H, HOSONO T, SAKAKI K, HAYASHI T, KIM Y A, ENDO M, MORIMOTO S, KOIDE A. Multi-walled carbon nanotube-reinforced magnesium alloy composites [J]. Scripta Materialia, 2008, 58: 267−270.

[12] LI C D, WANG X J, WU K, LIU W Q, XIANG S L, DING C, HU X S, ZHENG M Y. Distribution and integrity of carbon nanotubes in carbon nanotube/magnesium composites [J]. Journal of Alloys and Compounds, 2014, 612: 330−336.

[13] XIANG Shu-lin, WANG Xiao-jun, GUPTA M, WU Kun, HU Xiao-shi, ZHENG Ming-yi. Graphene nanoplatelets induced heterogeneous bimodal structural magnesium matrix composites with enhanced mechanical properties [J]. Scientific Reports, 2016, 6: 38824.

[14] CHEN Lian-yi, KONISHI H, FEHRENBACHER A, MA Chao, XU Jia-quan, CHOI H, XU Hui-fang, PFEFFERKORN F E, LI Xiao-chun. Novel nanoprocessing route for bulk graphene nanoplatelets reinforced metal matrix nanocomposites [J]. Scripta Materialia, 2012, 67: 29−32.

[15] SONG Jiang-feng, SHE Jia, CHEN Dao-lun, PAN Fus-heng. Latest research advances on magnesium and magnesium alloys worldwide [J]. Journal of Magnesium and Alloys, 2020, 8: 1−41.

[16] ZHOU Wei-wei, YAMAGUCHI T, KIKUCHI K, NOMURA N, KAWASAKI A. Effectively enhanced load transfer by interfacial reactions in multi-walled carbon nanotube reinforced Al matrix composites [J]. Acta Materialia, 2017, 125: 369−376.

[17] PARK Y, CHO K, PARK I, PARK Y. Fabrication and mechanical properties of magnesium matrix composite reinforced with Si coated carbon nanotubes [J]. Procedia Engineering, 2011, 10: 1446−1450.

[18] NAI M H, WEI J, GUPTA M. Interface tailoring to enhance mechanical properties of carbon nanotube reinforced magnesium composites [J]. Materials and Design, 2014, 60: 490−495.

[19] HAN Guo-qiang, DU Wen-bo, YE Xiao-xin, LIU Ke, DU Xian, WANG Zhao-hui, LI Shu-bo. Compelling mechanical properties of carbon nanotubes reinforced pure magnesium composite by effective interface bonding of Mg_2Ni [J]. Journal of Alloys and Compounds, 2017, 727: 963−969.

[20] YUAN Qiu-hong, ZENG Xiao-shu, WANG Yan-chun, LUO Lan, DING Yan, LI De-jiang, LIU Yong. Microstructure and mechanical properties of Mg−4.0Zn alloy reinforced by NiO-coated CNTs [J]. Journal of Materials Science & Technology, 2017, 33: 452−460.

[21] WU Li-qun, WU Rui-zhi, HOU Le-gan, ZHANG Jing-huai, ZHANG Mi-lin. Microstructure, mechanical properties and wear performance of AZ31 matrix composites reinforced by graphene nanoplatelets(GNPs) [J]. Journal of Alloys and Compounds, 2018, 750: 530−536.

[22] WANG Miao, ZHAO Yu, WANG Li-dong, ZHU Yun-peng, WANG Xiao-jun, SHENG Jie, YANG Zi-yue, SHI Hai-long, SHI Zhen-dong, FEI Wei-dong. Achieving high strength and ductility in graphene/magnesium composite via an in-situ reaction wetting process [J]. Carbon, 2018, 139: 954−963.

[23] YUAN Qiu-hong, HUANG Han-qing, WANG Wei-cheng, ZHOU Guo-hua, LUO Lan, ZENG Xiao-shu, LIU Yong. Achieving high stability of MgO/carbon nanotube interface via the co-deposition technique [J]. Journal of Alloys and Compounds, 2020, 824: 153889.

[24] YUAN Qiu-hong, ZENG Xiao-shu, LIU Yong, LUO Lei, WU Jun-bin, WANG Yan-chun, ZHOU Guo-hua. Microstructure and mechanical properties of AZ91 alloy reinforced by carbon nanotubes coated with MgO [J]. Carbon, 2016, 34: 843−855.

[25] YUAN Qiu-hong, ZHOU Guo-hua, LIAO Lin, LIU Yong, LUO Lan. Interfacial structure in AZ91 alloy composites reinforced by graphene nanosheets [J]. Carbon, 2018, 127: 177−186.

[26] KHOMYAKOV P A, GIOVANNETTI G, RUSU P C, BROCKS G, BRINK J, KELLY P J. First-principles study of the interaction and charge transfer between graphene and metals [J]. Physical Review B, 2009, 79: 195425.

[27] LIU Yang, WANG Gang, WANG Yi-ren, JIANG Yong, YI Dan-qing. Enhanced Cu/graphene adhesion by doping with Cr and Ti: A first principles prediction [J]. Transactions of Nonferrous Metals Society of China, 2019, 29: 1721−1727.

[28] DONG Er-ting, SHEN Ping, SHI Lai-xin, ZHANG Dan, JIANG Qi-chuan. Wetting and adhesion at Mg/MgO interfaces [J]. Journal of Materials Science, 2013, 48: 6008−6017.

[29] CHEN T, ZENG B, LIU J L, DONG J H, LIU X Q, WU Z, YANG X Z, LI Z M. High throughput exfoliation of graphene oxide from expanded graphite with assistance of strong oxidant in modified Hummers method [J]. Journal of Physics: Conference Series, 2009, 188: 012051.

[30] KRESSEAND G, FURTHMÜLLER J. Efficiency of ab-initio total energy calculations for metals and semiconductors using a plane-wave basis set [J]. Computational Materials Science, 1996, 6: 15−50.

[31] FURTHMÜLLER J, HAFNER J, KRESSE G. Ab initio calculation of the structural and electronic properties of carbon and boron nitride using ultrasoft pseudopotentials [J]. Physical Review B, 1994, 50(21): 15606.

[32] BLÖCHL P E. Projector augmented-wave method [J]. Physical Review B, 1994, 50(24): 17953−17979.
[33] PERDEW J P, BURKE K, ERNZERHOF M. Generalized gradient approximation made simple [J]. Physical Review Letters, 1996, 77(18): 3865−3868.
[34] GRIMME S. Semiempirical GGA-type density functional constructed with a long-range dispersion correction [J]. Journal of Computational Chemistry, 2006, 27(15): 1787−1799.
[35] HUH S H. Thermal reduction of graphene oxide [M]. London: InTech, 2011.
[36] SMITH J R, HONG T, SROLOVITZ D J. Metal−ceramic adhesion and the Harris functional [J]. Physical Review Letters, 1994, 72(25): 4021−4024.
[37] DU X M, ZHENG K F, CHEN R Q, LIU F G. First-principle study of the interaction between graphene and metals [J]. Digest Journal of Nanomaterials and Biostructures, 2017, 12(2): 463−471.

MgO 中间层增强 Mg/石墨烯界面结合性能的第一性原理预测和分析

王维澄[1]，刘金龙[1]，赵晗晗[1]，袁秋红[2]，罗 岚[1,3]，江 勇[4]，刘 勇[1]

1. 南昌大学 江西省轻质高强结构材料重点实验室，南昌 330031；
2. 宜春学院 物理科学与工程技术学院，宜春 336000；
3. 南昌大学 材料科学与工程学院，南昌 330031；
4. 中南大学 材料科学与工程学院，长沙 410083

摘 要：石墨烯增强镁基复合材料面临镁/石墨烯界面结合弱的难题。本文作者采用第一性原理计算评估通过引入原位生成的 MgO 中间层来改善 Mg/石墨烯结合的可行性。计算的界面结合强度由高到低的顺序为 Mg(0001)/$MgO(1\bar{1}1)$ > $MgO(1\bar{1}1)$/石墨烯 > Mg(0001)/石墨烯。Mg/MgO/石墨烯界面结合的增强可以归因于在 Mg/MgO 和 MgO/石墨烯界面上新形成的离子键和共价键的强烈相互作用取代了原来镁和石墨烯之间极弱的范德华力作用。

关键词：镁基复合材料；石墨烯；氧化镁；界面；第一性原理

(Edited by Wei-ping CHEN)